

1 **Colonic epithelial adaptation to EGFR-independent growth induces chromosomal instability and**  
2 **is accelerated by prior injury**

3

4 Tiane Chen<sup>1,2,\*</sup>, Maged Zeineldin<sup>1,2,\*</sup>, Blake Johnson<sup>2,3,4</sup>, Yi Dong<sup>2,3</sup>, Akshay Narkar<sup>2,3</sup>, Taibo Li<sup>4</sup>, Jin  
5 Zhu<sup>2,3</sup>, Rong Li<sup>2,3,5,6</sup>, Tatianna C. Larman<sup>1,2\*\*</sup>

6

7 <sup>1</sup>Department of Pathology, Division of GI/Liver Pathology, Johns Hopkins University School of  
8 Medicine, Baltimore, MD

9 <sup>2</sup>Center for Cell Dynamics, Johns Hopkins University School of Medicine, Baltimore, MD

10 <sup>3</sup>Department of Cell Biology, Johns Hopkins University School of Medicine, Baltimore, MD

11 <sup>4</sup>Medical Scientist Training Program, Johns Hopkins University School of Medicine, Baltimore, MD

12 <sup>5</sup>Department of Chemical and Biomolecular Engineering, Johns Hopkins University

13 <sup>6</sup>Mechanobiology Institute and Department of Biological Sciences, National University of Singapore

14 \*These authors contributed equally to this work

15 \*\*Correspondence: Tatianna C. Larman; 855 N Wolfe St, Rangos 453, Baltimore 21205; O (410-614-  
16 5143); F(410-955-0394); [tlarman1@jhmi.edu](mailto:tlarman1@jhmi.edu); @tashalarman

17

18 **RUNNING TITLE**

19 Adaptation to EGFR deficiency induces chromosomal instability in normal colonic epithelium

20

21

22 **FUNDING**

23 AACR Never Too Young Early Onset Colorectal Cancer Coalition (T.C.L.), Johns Hopkins Conte  
24 Digestive Diseases Basic and Translational Research Core Center Pilot Project Funding (T.C.L.), GI  
25 Cancer SPORE Pilot Project Funding (T.C.L.), Sanfilippo Resident Research Award (T.C.L.), Catherine  
26 and Constantinos J. Limas Research Award (T.C.L.), NIH Medical Scientist Training Program Award  
27 T32 GM007309 (B.J., T.L.).

28

29 **CONFLICT OF INTEREST**

30 The authors declare no competing interests.

31

32 **AUTHOR CONTRIBUTIONS**

33 Conceptualization, T.C.L., R.L.; Supervision, T.C.L. and R.L.; Investigation, T.C., M.Z., T.C.L., R.L.;  
34 Resources, A.N., B.J. T.L., and Y.D.; Data Curation, T.L.; Visualization, T.C., M.Z., T.L., B.J., T.C.L.;  
35 Validation, J.Z., M.Z.; Writing—Original Draft, T.C., T.C.L.; Writing—Review and Editing, T.C., M.Z.,  
36 T.C.L., R.L.; Funding acquisition, T.C.L., R.L.

37 **ABSTRACT**

38 Although much is known about the gene mutations required to drive colorectal cancer (CRC) initiation,  
39 the tissue-specific selective microenvironments in which neoplasia arises remains less characterized.  
40 Here, we determined whether modulation of intestinal stem cell niche morphogens alone can exert a  
41 neoplasia-relevant selective pressure on normal colonic epithelium. Using adult stem cell-derived  
42 murine colonic epithelial organoids (colonoids), we employed a strategy of sustained withdrawal of EGF  
43 and EGFR inhibition to select for and expand survivors. EGFR-signaling-independent (iEGFR)  
44 colonoids emerged over rounds of selection and expansion. Colonoids derived from a mouse model of  
45 chronic mucosal injury showed an enhanced ability to adapt to EGFR inhibition. Whole-exome and  
46 transcriptomic analyses of iEGFR colonoids demonstrated acquisition of deleterious mutations and  
47 altered expression of genes implicated in EGF signaling, pyroptosis, and CRC. iEGFR colonoids  
48 acquired dysplasia-associated cytomorphologic changes, an increased proliferative rate, and the ability  
49 to survive independently of other required niche factors. These changes were accompanied by  
50 emergence of aneuploidy and chromosomal instability; further, the observed mitotic segregation errors  
51 were significantly associated with loss of interkinetic nuclear migration, a fundamental and dynamic  
52 process underlying intestinal epithelial homeostasis. This study provides key evidence that  
53 chromosomal instability and other phenotypes associated with neoplasia can be induced *ex vivo* via  
54 adaptation to EGF withdrawal in normal and stably euploid colonic epithelium, without introducing  
55 cancer-associated driver mutations. In addition, prior mucosal injury accelerates this evolutionary  
56 process.

57 **Keywords**

58 Intestinal organoids; transformation; chromosomal instability; colorectal cancer; colitis

59

60 **Key definitions:**

61 Colonoids: adult stem cell-derived colonic epithelial organoids

62 iEGFR: *in vitro* selective conditions devoid of EGF (epidermal growth factor) and including an EGFR  
63 (EGF receptor) inhibitor<sup>1</sup>

64 iEGFR colonoids: colonoids tolerant to iEGFR culture conditions with growth and survival similar to  
65 unselected passage-matched controls

66 INM: Interkinetic nuclear migration

67

68

## 69 INTRODUCTION

70 While much is known about the molecular features of CRC and their adenomatous precursors, it  
71 remains a mystery how neoplasia arises from normal epithelium<sup>2,3</sup>. The colonic epithelial crypt is a test-  
72 tube shaped unit comprised of Lgr5<sup>+</sup> stem cells at its base, with its differentiation axis determined by  
73 epithelial and stromal microenvironment-derived gradients of niche growth factors<sup>4-6</sup>. How perturbations  
74 to normal niche growth factor homeostasis may act to promote or constrain initiation of epithelial  
75 neoplasia remain largely unexplored.

76 Advances in intestinal organoid culture have provided profound insights into the niche signaling  
77 pathways required for maintenance of epithelial homeostasis, including the EGFR/MAPK, Wnt, Notch,  
78 PI3K, and TGF- $\beta$  pathways<sup>7</sup>. Intriguingly, these same pathways are recurrently altered in colorectal  
79 cancer (CRC), which is in turn characterized by epithelial architectural complexity, niche remodeling,  
80 and progressive loss of dependence on key niche factors<sup>2,3,8,9</sup>. Organoid cultures derived from  
81 adenomatous precursors and CRC demonstrate heterogeneous patterns of niche factor-independent  
82 growth reflective of underlying molecular changes<sup>3,8</sup>. For example, unlike normal epithelial cells, the  
83 vast majority of adenoma and CRC cells grow independently of Wnt and R-spondin *ex vivo*,  
84 underscoring the fact that *APC* mutation is a common first hit<sup>3</sup>. Further, multiple groups have leveraged  
85 the intestinal organoid model to reconstitute the adenoma-carcinoma sequence *in vitro*, harnessing  
86 selective strategies to identify successfully edited clones; for example, *KRAS* or *PIK3CA* mutant  
87 organoids survive in EGF-deficient conditions<sup>10-12</sup>.

88 The positioning of cells in the intestinal crypt dictates cell fate<sup>13</sup>. Interkinetic nuclear migration (INM) has  
89 recently been shown to contribute to the dynamics of cell positioning in the intestinal crypt<sup>14</sup>. INM is a  
90 homeostatic mitotic mechanism in intestinal epithelium by which basally located nuclei migrate to the  
91 apical aspect of the cell for mitosis, then return to a basal cytoplasmic location after separation of  
92 mitotic sisters<sup>14</sup>. Interestingly, loss of INM in *Apc* mutant murine intestinal organoids resulted in  
93 placement of mitotic sisters directly adjacent to one another, rather than the physically separated  
94 mitotic sisters seen in wild-type mitoses with intact INM<sup>14</sup>. Thus, in addition to altered niche growth  
95 factor homeostasis, biophysical factors related to mitotic dynamics, cell geometry, and/or  
96 microenvironmental stiffness may also directly contribute to clonal expansion of crypt cell populations to  
97 promote neoplasia. In the human colon, cycles of mucosal injury and repair (for example, in  
98 inflammatory bowel disease, or IBD) can transiently or permanently alter the biophysical properties, cell  
99 populations, and growth factors present in the mucosal microenvironment<sup>15</sup>. Although the mechanisms

100 are not fully elucidated, such chronic inflammatory insults lead to increased risk for CRC and other  
101 epithelial cancers<sup>16,17</sup>.

102 Here we tested the hypothesis that disturbances to the mucosal microenvironment alone have capacity  
103 to lead to epithelial-autonomous molecular changes promoting cancer. As the feasibility of short-term  
104 EGF withdrawal in organoid culture has been demonstrated<sup>1</sup>, EGF is a critical intestinal stem cell niche  
105 factor<sup>7,18–20</sup>, and EGF signaling is indispensable for normal intestinal stem cell survival and propagation  
106 *in vitro*<sup>3,7</sup>, we focused our selection experiments on the evolution of EGFR-signaling-independent  
107 growth. Indeed, our data show that long-term withdrawal of EGFR signaling alone results in a  
108 molecularly distinct and sustained adaptive epithelial phenotype.

109

110

111

112

113

114

115

116

117

118

119

120

121

122

123

124

## 125 **METHODS**

### 126 **Mouse Strains Used to Derive Colonoid Lines**

127 Primary colonoid cultures used in this study were derived from C57BL/6J mice (directly received from  
128 Jackson Laboratory). All animal experiments were implemented in accordance with an animal protocol  
129 approved by the Johns Hopkins University Animal Care and Use Committee (Protocol MO18M85) and  
130 ARRIVE (Animal Research: Reporting of *In Vivo* Experiments) guidelines. All the mice were housed in  
131 a specific pathogen-free (Helicobacter negative) environment. The DSS chronic colitis mouse model  
132 was established as has been described previously with minor modifications<sup>21-23</sup>. In short, male mice 6-8  
133 weeks old were treated with 4 rounds of DSS challenge, each consisting of 5 days of DSS in drinking  
134 water (2%, 40 kDa) followed by 7 days of recovery (Alfa Aesar #J63606).

### 135 **Colonoid Culture**

136 We derived colonoids from normal wildtype C57BL/6 mice (referred to hereafter as control colonoids).  
137 Colonoids were derived from the distal 2.5 cm of grossly normal appearing C57BL/6J mouse colons  
138 (females 26 weeks old for control and *Apc*<sup>mut</sup> colonoid lines). Absence of deleterious coding mutations  
139 was confirmed by whole-exome sequencing (data not shown). Notably, mouse colons lack Paneth  
140 cells, a potential source of EGF<sup>24</sup>. Colonic crypts were isolated and cultured as described previously<sup>7,10</sup>.  
141 Colonoids were plated within Matrigel (Corning #356231). Basic culture medium was composed of  
142 advanced Dulbecco's modified Eagle's medium/F12 (Gibco™) supplemented with  
143 penicillin/streptomycin, 10 mM HEPES (Gibco™ #15630080), GlutaMAX supplement (Gibco™  
144 #35050061), B27™ Supplement (Gibco™ #17504044) and 1 mM N-acetylcysteine (Sigma-Aldrich  
145 #A9165). WENR medium was made of basic culture medium (20% final volume), Wnt3a-conditioned  
146 media (50% final volume with 5% final FBS concentration, L Wnt-3A ATCC® CRL-2647), and R-  
147 Spondin1-conditioned media (20% final volume), Noggin-conditioned media (10% final volume) and  
148 EGF (50 ng/mL). WNR medium had EGF omitted. Colonoids were maintained and propagated in  
149 culture as described previously<sup>7</sup>.

### 151 **Colonoid transfection and genome editing**

152 The colonoid lipofection and CRISPR/Cas9 genome editing protocol was followed as described  
153 previously<sup>25,26</sup>. The sgRNA sequence targeting *Apc* can be found in Supplementary Figure 3A. As  
154 described previously, single colonoid survivors in Wnt/R-spondin-deficient media were manually picked  
155 and clonally expanded under the same selective conditions. The presence of biallelic truncating  
156 mutations at the expected site was confirmed by Topo cloning and whole-exome sequencing  
157 (Supplementary Figure 3B). Off-target coding mutations were not detected (data not shown).

## 158 **Derivation of iEGFR-tolerant organoids**

159 Three days after plating in Matrigel, passage-matched colonoids were switched from WENR to iEGFR  
160 media (WNR with 5  $\mu$ M Gefitinib; Santa Cruz #sc-202166). This concentration of gefitinib was required  
161 to kill >90% of normal colonoids at 7 days (data not shown) and was previously used to achieve iEGFR  
162 intestinal organoid culture conditions<sup>1</sup>. Fresh media with the drug was added every other day. Survivors  
163 were collected after 7 days and allowed to expand in WNR media before re-challenging in iEGFR  
164 selection for another 7 days. These cycles of selection and expansion were repeated until the survival  
165 rate plateaued (iEGFR-tolerant colonoids). All control colonoids were treated with similar concentration  
166 and volume of the compound dissolvent, dimethyl sulfoxide (DMSO, Corning® #25-950-CQC). Control  
167 colonoids were maintained in WENR media, and iEGFR-tolerant colonoids were maintained in WNR  
168 media long-term. Brightfield images of each cycle were captured on day 0 and day 7 using a Zeiss  
169 Microscope (Carl Zeiss Axiovert 40 C) with a 4x objective and the iDu Optics LabCam Microscope  
170 Adapter for iPhone8+ (iDu Optics). Quantification of survival rate was carried out manually. At the  
171 beginning of each cycle, the total number of colonoids in both control and treatment groups were  
172 counted under the microscope with a cell counter based on visual inspection (see images in  
173 Supplementary Figure 3D). At the end of each selection cycle (7 days), the total number of live  
174 colonoids in each well of both groups was counted. Survival rate was calculated as the total number of  
175 live colonoids post-treatment at day 7 to total number of colonoids pre-treatment at day 0 in each well.  
176 The relative survival rate was generated by comparing survival to untreated controls.

177

## 178 **Histology**

179 Whole colonoids were collected by gently dissolving Matrigel in ice-cold PBS (pH 7.4), and  
180 subsequently fixed for 30 min at room temperature in 4% paraformaldehyde (16% PFA, Pierce™  
181 #28906). Colonoids were then washed with PBS (pH 7.4) at room temperature. Colonoids were  
182 pelleted and transferred to the top of 2% solidified agarose gel in a 0.5 mL microfuge tube (Sigma-  
183 Aldrich #A9539). After aspiration of PBS, another 100 $\mu$ L of warm agarose gel was added to the  
184 colonoids. After gel solidification, the entire microcentrifuge tube was placed into a 15 mL conical  
185 containing 10 mL buffered 10% formalin (Sigma-Aldrich #HT501128) overnight. The bottom of the  
186 microcentrifuge tube was carefully removed with a razor blade and the colonoid block was transferred  
187 into a tissue cassette and submitted for paraffin embedding. 4  $\mu$ m thick sections were stained with  
188 hematoxylin and eosin (performed by the Johns Hopkins Oncology Tissue Services Core).  
189 Photomicrographs of colonoids and deidentified human tissue samples (in accordance with the Johns  
190 Hopkins University School of Medicine Institutional Review Board, IRB00273344) were taken using an  
191 Olympus BX46 upright microscope and Teledyne Lumenera Infinity Analyze software.

## 192 **Metaphase spreads**

193 Colonoids were treated with 100  $\mu$ M colcemid (Gibco™ #15212012) for 4 hours and dissociated with  
194 800  $\mu$ L of TrypLE (Gibco™ #12604013) and Accutase (Invitrogen™ #00-4555-56) (1:1 ratio) for 10–15  
195 min at 37 °C. After washout of TrypLE and accutase with advanced DMEM/F12 medium (Gibco™  
196 #12634010) containing HEPES buffer (Gibco™ #15630080, 1 mM), penicillin/streptomycin (Gibco™  
197 #15140122, 1%), GlutaMax (Gibco™ #35050061, 0.2 mM), cells were treated with pre-warmed KCl  
198 (0.56%) for 15 min at room temperature. Subsequently, 120  $\mu$ l of fixative solution (methanol:acetic acid;  
199 3:1) were added before centrifuging. After centrifugation, 10 ml fixative solution were slowly added  
200 before incubation at 4°C overnight. Fixed cells were dropped onto a glass microscope slide using a 20-  
201  $\mu$ l pipette, air dried, and heat-dried (65°C) for 60 min. Slides were then incubated for 1 hour at 37 °C in  
202 propidium iodide (PI)/RNase staining buffer and rinsed with ddH<sub>2</sub>O. Slides were mounted with  
203 Vectashield containing DAPI (Vector Labs #H-1000) and analyzed on a Nikon laser microscope ( $\times$ 60  
204 Super-Plan APO oil 1.4 NA objective). Control colonoids were assayed at passages 8 and 15; iEGFR  
205 colonoids were assayed at passage 40 (low, L) and passage 66 (high, H); *Apc*<sup>mut</sup> colonoids were  
206 assayed at passages 28 and 30; DSS control colonoids were assayed at passages 5, 15, and 35; and  
207 DSS iEGFR colonoids were assayed at passages 15 and 35. Results were similar across passage  
208 numbers and combined per group, with the exception of iEGFR colonoids (as noted in Figure 4A).  
209 Chromosomes from each spread were manually counted in a blinded manner using Fiji/ImageJ.

210

## 211 **3D immunostaining and clearing of organoids**

212 Whole colonoids were collected by gently dissolving Matrigel in ice-cold PBS and fixed for 30 min at  
213 room temperature in 4% paraformaldehyde (PFA, Sigma). Colonoids were then transferred to organoid  
214 washing buffer (PBS containing 0.1% Triton X-100 and 0.2% BSA), then distributed into a 24-well plate.  
215 For immunofluorescent staining, colonoids were permeabilized and blocked in PBS containing 0.5%  
216 Triton X-100 and 1% BSA (Sigma) for 1 hour at room temperature, then incubated in blocking buffer  
217 containing primary antibody overnight at 4°C. Primary antibodies used were Chromogranin A (Santa  
218 Cruz #Sc-1488) and phospho-histone H2A.X (Ser139; Cell Signaling Tech #2577). Colonoids were  
219 incubated with corresponding secondary antibody Alexa 488 anti-mouse IgG (Invitrogen™ #A11029), in  
220 blocking buffer for overnight at 4°C, with 1 $\mu$ g/ $\mu$ l DAPI added for the final 15 minutes of incubation.  
221 Colonoids were washed 4-5 times (2 hours each), then cleared in fructose-glycerol clearing buffer (60%  
222 (vol/vol) glycerol and 2.5 M fructose) for 15 mins before imaging on a Zeiss LSM 780 confocal  
223 microscope<sup>27</sup>. Image analysis was performed using Zen and Fiji/ImageJ software.

224

225

## 226 **EdU incorporation assay**

227 Colonoids were plated in an 8-well Chamber Coverglass (Nunc™ Lab-Tek™, Cat#155411). 4-5 days  
228 after plating, EdU (10 μM) was added to fresh medium for 6 hours. Colonoids were then fixed with  
229 warm 4% PFA for 10 mins at 37°C, then rinsed once with room temperature PBS. Blocking and  
230 permeabilization buffer (PBS containing 1% BSA and 0.5 % Triton X-100) was added for 2 hours at  
231 room temperature. EdU detection reagents were then added for 2 hours at room temperature in the  
232 dark (Click-iT™ Assay Kit, Sigma-Aldrich #C10337). Nutlin was used as a positive control (Selleckchem  
233 #S7101). Images were captured with the Zeiss LSM780 confocal microscope (40x/1.4 NA objective).  
234 Image analysis was performed using Zen, Fiji/ImageJ and Imaris software.

235

## 236 **Four-dimensional colonoid imaging and image analysis**

237 **Lentivirus production:** The plasmids used were pMD2.G (Addgene plasmid RRID# 12259), psPAX2  
238 (Addgene plasmid RRID#12260), and pLV-H2B-Neon-ires-Puro (kindly gifted by the Hugo J.G. Snippert  
239 and Geert J.P.L. Kops laboratories of the University Medical Center Utrecht). To make lentivirus  
240 particles, HEK 293FT cells were co-transfected with the lentiviral transfer plasmid, packaging plasmid,  
241 and envelope plasmid. Media containing lentivirus was collected 24 and 48 hours after transfection.  
242 Lentivirus was concentrated using a centrifugal filter (Amicon Ultra-15, 100,000 NMWL). The lentiviral  
243 titer was determined by qPCR (abm qPCR Lentivirus Titration Kit, cat. # LV900). Viral titers used in this  
244 study ranged from  $1 \times 10^8$ - $1 \times 10^9$  IU/ml.

245

246 **Lentiviral infection of colonoids:** To visualize mitoses, colonoids were infected with lentivirus  
247 encoding mNeon-tagged histone 2B and a puromycin resistance cassette described above. The  
248 protocol was performed as described previously with minor modifications<sup>28</sup>. Briefly, colonoids ~100 μm  
249 in diameter were transferred to a 15 ml tube and pelleted (1000 rpm for 5 minutes) before single cell  
250 dissociation (600-800 μL TrypLE, 37°C). Pelleted single cells were resuspended in 1 ml of prewarmed  
251 infection medium, consisting of 500 μL concentrated virus, 500 μl WENR (control colonoids), WNR  
252 (iEGFR colonoids), or Wnt/R-spondin deficient media (*Apc<sup>mut</sup>* colonoids), 8 μg/ml Polybrene (Sigma-  
253 Aldrich #TR-1003), and 10 μM Rock inhibitor Y-27632 (Sigma-Aldrich #Y0503), then centrifuged at 100  
254 rpm for 1h at room temperature. Colonoids were then transferred to the cell incubator (37°C, 5% CO<sub>2</sub>)  
255 for 5–6 hours and gently remixed every hour prior to replating with fresh media as indicated.  
256 Approximately 2-3 days after infection, the expression of transduced fluorescence protein was  
257 observed and puromycin selection (1 μg/mL) was initiated. Puromycin was increased to 5ug/mL once  
258 colonoid size reached more than 100 μm.

259



260 **Four-dimensional colonoid imaging:** After two passages of puromycin selection, colonoids were  
261 dissociated using TrypLE and replated in an 8-well glass-bottom chamber slide (Nunc™ Lab-Tek™,  
262 Cat#155411). Three to four days later, the chamber was mounted on a confocal laser-scanning  
263 microscope (LSM 780), which was continuously held at 37 °C with 5.0% CO<sub>2</sub>. H2B-Neon-positive  
264 organoids were imaged in xyzt mode for 16–18h at 37°C at 3 min intervals using a 40x water-  
265 immersion objective (NA 1.1). Eight to ten H2B-mNeon-expressing colonoids were imaged  
266 simultaneously using minimal amounts of 488 nm laser excitation. In total, 14-16 z-sections at 2-µm  
267 intervals were imaged per colonoid.

268

269 **Imaging analysis:** To analyze mitoses, raw image Z-stacks were converted to depth color-coded  
270 maximum projections with using a custom macro modified from the ImageJ/Fiji software plugin  
271 “Temporal-Color Code”<sup>29</sup>. The macro attributes a color code to each z-layer, facilitating visual  
272 discrimination of cells overlapping in XY as described previously<sup>10</sup>. Data sets were converted into  
273 manageable and maximally informative videos, combining z-projection, depth color-coding and merging  
274 with transmitted light images (Supplementary Videos 1–6). Mitoses were blinded and scored, judged  
275 and counted manually by both T.C. and T.C.L. For analysis of interkinetic nuclear migration, Fiji/ImageJ  
276 was used to measure the pixel distance the basal aspect of a nucleus moved prior to mitotic entry and  
277 nuclear envelope breakdown. Any distance moved was categorized as intact interkinetic nuclear  
278 migration. No measurable movement was categorized as loss of interkinetic nuclear migration.

279

### 280 **Quantitative RT-PCR based mouse karyotyping**

281 SYBR Green qPCR assays were designed and validated for every mouse chromosome based on  
282 GRCm38/mm10 genome assembly (primer sequences listed in Table S1). qPCR reactions were set up  
283 in triplicate in a 384-well plate and run on the CFX384 Touch Real-Time PCR Detection System (Bio-  
284 Rad). Each reaction contained 5µL of PerfeCTa SYBR Green FastMix (Quantabio, catalog number  
285 95073-05K), 2.5µL of forward and reverse primer mix at 2µM, 0.5µL of purified genomic DNA at 1ng/µL  
286 and 2µL of nuclease-free water. A standard cycling protocol was followed as provided with the SYBR  
287 Green reagent. Ct values were acquired with CFX Manager Software (Bio-Rad) and the relative  
288 chromosome copy numbers were calculated using a modified  $\Delta\Delta C_t$  method as described previously<sup>30</sup>.

289

### 290 **RNA sequencing**

291 Total RNA was isolated from pelleted colonoids in using Trizol (Invitrogen™ #15596026) according to  
292 the manufacturer’s instructions and purified using the Purelink RNA Mini Kit (Invitrogen™ #12183018A).  
293 RNA-sequencing data were generated by Novogene. cDNA libraries were sequenced on an Illumina

294 NextSeq500 using 75-bp paired-end sequencing. Clean reads were mapped to UCSC GRCm38  
295 reference genome using STAR v2.5 software<sup>31</sup> and raw counts were assigned to Ensembl genes using  
296 featureCounts (subread v2.0.0 aligner command line tool)<sup>32</sup>. Differential gene analysis was performed  
297 using DESeq2 v1.28.1 following regularized logarithm transformation of raw count data<sup>33</sup>. Gene set  
298 enrichment analysis (GSEA) was performed using the gost function of the R package gprofiler2  
299 v0.1.9<sup>34</sup>. Genes were considered differentially expressed and included in the GSEA if they had a *p*-  
300 value <3.3e-7 (Bonferroni adjusted) and an absolute log<sub>2</sub>-transformed fold change >2. Statistical  
301 analysis and plotting were performed using R software (version 3.4.0). Statistical significance was  
302 assessed at  $\alpha=0.05$ . The significance level for differential gene analysis was adjusted using the  
303 Bonferroni approach while also accounting for multiple comparisons across experimental conditions  
304 (threshold  $p=3.3e-7$ ). All data are presented as mean  $\pm$  SEM. Analysis of two samples was performed  
305 with unpaired two-tailed student t-test for equal variance, or t-test with Welch's correction for  
306 heterogeneity of variance.

307

### 308 **Whole Exome sequencing**

309 DNA was extracted from pelleted colonoids using the Purelink Genomic DNA Kit (Invitrogen™ #K1820-  
310 01) according to the manufacturer's instructions. Whole exome sequencing data were generated by  
311 BGI. In short, fragmented gDNA was subjected to adapter ligation, amplification, and exome array  
312 hybridization. Captured products were circularized and DNA nanoballs were produced using rolling  
313 circle amplification prior to loading onto the BGISEQ sequencing platform. Mean sequencing depth on  
314 target regions was 117.58x, and 98.69% of targeted bases had at least 10x coverage. Paired-end  
315 reads were mapped to UCSC GRCm38 and aligned using Burrows-Wheeler Aligner (BWA) software.  
316 The Genome Analysis Toolkit (GATK) was used for variant calling and the SnpEff tool was used for  
317 variant annotation. Variants of interest were filtered based on >10x depth of coverage, predicted high  
318 functional impact (MutDB), and visual inspection using Integrative Genomics Viewer (IGV).

319

### 320 **Quantitative RT-PCR**

321 cDNA was isolated using SuperScript™ III Reverse Transcriptase (Invitrogen # 108080) following the  
322 manufacturer's protocol. A dilution series of cDNA was used to validate the primer pairs, and both  
323 melting curve analysis and agarose gel electrophoresis were performed to check for specificity of  
324 primers (data not shown). Quantitative PCR was performed using the SYBR green Select Master Mix  
325 (Thermo Fisher #4472908) following the manufacturer's protocol. Each sample was done in triplicate in  
326 a total reaction volume of 10- $\mu$ l containing 0.5- $\mu$ l of 1:8 diluted cDNA (validated dilution with dynamic  
327 range of amplification) and 5nM primer mix using the CFX384 QPCR machine (Biorad). The list of

328 primers used are listed in Supplementary Table 3. Delta (Cq) was calculated by subtracting the mean  
329 Cq for every tested gene to those of the internal control genes (*Hprt* and *ActB*). Log fold change was  
330 calculated by subtracting Delta(Cq) of iEGFR samples from those of controls.

331

332

333

334

335

336

337

338

339

340

341

342

343

344

345

346

347

348

349

350

## 351 RESULTS

### 352 Normal murine colonoids can achieve sustained EGFR-independent growth in long-term culture

353 We tested our hypothesis that changes in the availability of niche factors can select for a cancer  
354 phenotype in normal wild-type colonic epithelium using colon-derived organoids (colonoids). To select  
355 for EGFR-independent growth *in vitro*, we cultured normal colonoids from wild-type mice (“control”  
356 colonoids) in EGF-depleted (WNR) medium with the EGFR-specific inhibitor Gefitinib; we refer to these  
357 culture conditions as iEGFR. The EGFR inhibitor was used to address the possibility of  
358 autocrine/paracrine production of EGF by the cultured colonoids or the presence of exogenous EGF in  
359 the 5% final concentration of fetal bovine serum in EGF-depleted medium. Over 7 days, iEGFR  
360 selection resulted in the death of most colonoids. Rare survivor colonoids appeared smaller and lacked  
361 budding compared to control colonoids, suggesting that they were mostly quiescent<sup>1</sup>. These survivors  
362 were recovered and expanded in WNR media, but not in the presence of Gefitinib. We continued to re-  
363 challenge the expanded survivors with additional 7-day cycles of iEGFR selection. Increasing numbers  
364 of survivors were recovered with each re-challenge cycle (Figure 1A), and approximately half of  
365 colonoids survived after 3 cycles of selection. A total of 5 cycles were required to achieve complete  
366 EGFR-independent growth (iEGFR colonoids), with survival rate similar to unchallenged colonoids in  
367 EGF-replete media (Figure 1A). Notably, we also observed a transient enrichment of cells with  
368 enteroendocrine differentiation during iEGFR selection as reported previously (Supplementary Figures  
369 1A-B)<sup>1</sup>. We continuously propagated iEGFR colonoids for 8 months in WNR medium.

370

371 To test whether iEGFR tolerance was reversible after relaxing selective conditions, we returned iEGFR  
372 colonoids to EGF-replete medium (WENR) for 3 weeks. Surprisingly, approximately 70% of iEGFR  
373 colonoids died each week in the presence of EGF compared to those maintained in the WNR medium.  
374 Moreover, removal of EGF from the culture reverted to the growth of iEGFR colonoid baseline of near-  
375 100% survival (Supplemental Figure 1C). Taken together, our data demonstrate the feasibility of  
376 evolving and propagating growth factor-independent colonic epithelium. They also show that the  
377 resulting phenotype is a stable trait that does not require persistent selection once acquired with an  
378 acquired and related vulnerability.

379

### 380 Prior epithelial injury facilitates adaptation to iEGFR selection

381 We tested whether chronic injury and repair can influence adaptability to EGF deprivation using  
382 colonoids generated from a mouse model of chronic chemical colitis (DSS, dextran sodium sulfate). As  
383 previously described<sup>35</sup>, these mice showed cardinal signs of colitis as manifested by a significant

384 reduction in the ratio between body weight to colon length (Supplementary Figure 2A) and histologic  
385 features (Supplementary Figure 2B). Colonoids derived from DSS-treated mice more readily adapted to  
386 iEGFR selection compared to controls, with approximately 60% of colonoids surviving the first 7 day  
387 cycle of selection compared to approximately 10% of control colonoids (Figure 1A). In addition, DSS  
388 colonoids reached a survival plateau after only 2 cycles of iEGFR selection (Figure 1B), compared to 5  
389 cycles for control colonoids. These data indicate that prior exposure to cycles of mucosal injury *in vivo*  
390 primed colonic epithelium for adaptation to iEGFR selection.

391

### 392 **iEGFR colonoids acquire tolerance to deprivation of other niche factors**

393 To test whether iEGFR colonoids more readily acquire additional niche factor independence, we  
394 challenged them in medium lacking Wnt/R-spondin, as well as in a base medium that additionally lacks  
395 Noggin. The majority of iEGFR colonoid lines survived this selective challenge after a week (Figure 1B,  
396 Supplementary Figure 3D). On the other hand, the majority of control colonoids did not survive either  
397 condition. These data demonstrate that iEGFR colonoids acquired the capacity to tolerate additional  
398 niche-relevant selective pressures.

399

### 400 ***Apc* mutant colonoids are more vulnerable to EGF-deficient conditions**

401 Mathematical modeling of CRC carcinogenesis suggests that *APC* mutations may accelerate the  
402 acquisition of subsequent molecular alterations<sup>36</sup>. If iEGFR adaptation relies upon *de novo* oncogenic  
403 mutation, *Apc* loss should confer an adaptive advantage. To test this hypothesis, we introduced biallelic  
404 truncating mutations in *Apc* via CRISPR/Cas9 genome editing to a control mouse colonoid line  
405 (Supplementary Figure 3A-B, confirmed by whole exome sequencing). As previously described, *Apc*  
406 mutant (*Apc*<sup>mut</sup>) colonoids grew independently of Wnt/R-spondin-containing medium and adopted  
407 spheroid morphology (Figure 1B and Supplemental Figure 3C)<sup>25</sup>. Surprisingly, when *Apc*<sup>mut</sup> colonoids  
408 were subjected to cycles of iEGFR selection, unlike wild type colonoids, *Apc*<sup>mut</sup> colonoids could not  
409 adapt to EGF deprivation (Figure 1A). These data suggest that *Apc* loss greatly enhances the  
410 sensitivity of colonoids to EGFR deprivation.

411

### 412 **iEGFR colonoids acquire somatic mutations and transcriptional reprogramming**

413 To determine whether mutations associated with EGF-independent growth may have contributed to the  
414 iEGFR phenotype, we performed whole exome sequencing on iEGFR colonoids and controls. First, we  
415 looked at mutations in the EGFR signaling pathway that are frequently observed in CRC. No mutations  
416 or indels in *Egfr*, *Kras*, or *Pik3ca* were detected in iEGFR colonoids. However, we detected a coding  
417 mutation with predicted high functional impact in *Wnk2*, a negative regulator of EGF-induced activation

418 of ERK/MAPK signaling<sup>37</sup>. iEGFR colonoids also showed predicted deleterious mutations in *Btk*, known  
419 to have a role in negatively regulating Wnt- $\beta$ -catenin signaling<sup>38</sup>, *Trem12*, and *Olf1255* (Table 1). Mining  
420 publicly available data reveals that these genes are altered at very low frequency (<1%) in human  
421 CRC, with the exception of *Olf1255* (Table 1). DSS iEGFR colonoids were enriched for a mutation in  
422 *Ninein* (Table 1), a gene involved in centrosomal biology and mitotic fidelity<sup>39</sup>. DSS colonoids did not  
423 accumulate coding mutations compared to control colonoids.

424

425 We also performed RNA-sequencing to explore the molecular changes in iEGFR, DSS iEGFR lines,  
426 and passage-matched controls. Principal component analysis established that replicate samples  
427 clustered together with high reproducibility (Figure 2A). We found a total of 547 differentially expressed  
428 genes in both types of iEGFR colonoids (absolute log<sub>2</sub> fold change >2, Bonferroni-adjusted p-value <  
429 0.05, Figure 2B, Supplementary Table 1, Supplementary Figure 4). Gene set enrichment analysis of the  
430 upregulated overlapping genes (48) showed significant enrichment for genes associated with amine  
431 transmembrane transporter activity, pyroptosis, and phosphatidylinositol-4-phosphate binding  
432 pathways, while the overlapping downregulated genes (22) were involved in endocytosis and cell  
433 junction assembly (Figure 2C). A subset of significantly differentially expressed genes was further  
434 validated using quantitative reverse transcription polymerase chain reaction (qRT-PCR), including  
435 those with roles in the EGF pathway, pyroptosis, and CRC carcinogenesis, such as *Igf1b7*, *Efemp1*,  
436 *Gasdmc2*, and *Mycn* (Figure 2D; all tested genes validated). Taken together, these data show that key  
437 neoplasia-relevant gene expression patterns emerge in colonic epithelial cells tolerant to EGF  
438 withdrawal.

### 439 **iEGFR colonoids exhibit morphologic changes and increased proliferation**

440 Early epithelial neoplasia demonstrates characteristic morphological changes that have been routinely  
441 used by pathologists to diagnose dysplasia and cancer for over a century<sup>40</sup>. Hematoxylin-and-eosin-  
442 stained iEGFR colonoids show heterogeneous morphologic changes associated with dysplasia,  
443 including nuclear hyperchromasia, pseudostratification, and increased nuclear-to-cytoplasmic ratio  
444 (Figure 3A). DSS control colonoids showed features of reactive and regenerative epithelium, including  
445 more squamoid cells with brightly eosinophilic cytoplasm. A subset of DSS iEGFR colonoids strikingly  
446 showed loss of polarity and architectural complexity reminiscent of high-grade colitis-associated  
447 dysplasia seen in patients with IBD (Figure 3A).

448 Neoplasia is also associated with sustained proliferation<sup>41</sup>. Our RNA-sequencing analysis revealed that  
449 many genes associated with cellular proliferation were upregulated in iEGFR colonoids, including the  
450 proto-oncogene *Mycn* (Figure 2D, Supplementary Table 1). To further explore this, we used a short-

451 pulse (6 hours) of the nucleotide analogue 5'-ethynyl-2'deoxyuridine (EdU) to analyze the proportion of  
452 cells in the S-phase of the cell cycle in iEGFR colonoids. The proportion of EdU+ colonoids and percent  
453 of EdU+ cells per colonoid were significantly higher in both iEGFR and DSS iEGFR colonoids  
454 compared to their controls (Figure 3B-3D). These data show that the iEGFR phenotype is characterized  
455 by histologic features of dysplasia and increased proliferation.

#### 456 **iEGFR colonoids develop aneuploidy and chromosomal instability**

457 Loss of genomic integrity is one of the hallmarks of cancer, and chromosomal instability (CIN, or  
458 ongoing aneuploidy) is observed in the majority of sporadic and IBD-associated CRC<sup>2,41</sup>. As aneuploidy  
459 fuels adaptation to selective pressures<sup>30,42</sup>, we hypothesized that this may play a role in acquisition of  
460 iEGFR tolerance. As the long-term genetic stability of adult stem cell derived intestinal organoid  
461 cultures has been established<sup>43</sup>, as expected, metaphase spreads of control organoids were mostly  
462 euploid (Figure 4A-B). In contrast, DSS-control colonoids were enriched for polyploidy (Figure 4A-B).  
463 Previous literature has implicated *APC* loss in promoting CIN<sup>44</sup>; we observed both polyploidy and  
464 aneuploidy in metaphase spreads of *Apc*<sup>mut</sup> colonoids (Figure 4A).

465 We observed that heterogenous aneuploidy arose during iEGFR selection, with an overall tendency for  
466 reduction in chromosomal number (subdiploid) (Figure 4A). Longer-term propagation of iEGFR  
467 colonoids (more than 25 additional passages) resulted in convergence onto a gain of one chromosome  
468 (Figure 4A, iEGFR 'H', or high passage)). Quantitative chromosome stoichiometry analysis via  
469 quantitative PCR revealed a complete loss of chromosome 13 at an earlier passage (~12 passages  
470 earlier than iEGFR 'H', Supplementary Figure 5). We hypothesized that aneuploidy could be due to  
471 increased DNA damage, but did not detect increased double stranded breaks as assessed by  $\gamma$ H2AX  
472 staining in iEGFR colonoids relative to their corresponding controls (Supplemental Figure 6).

473 We next investigated the possibility that the heterogeneous aneuploidy was associated with ongoing  
474 CIN. The dynamic properties of mitosis were quantified via live-imaging of 3D colonoid cultures of H2B-  
475 mNeon expressing cells (Figure 4C-F, Supplementary Videos 1-6). The mean length of mitosis in  
476 control colonoids was ~30 minutes, with errors detected in only 3-5% of all mitotic events (Figure 4C-D,  
477 H). In contrast, iEGFR, *Apc*<sup>mut</sup>, DSS control, and DSS iEGFR colonoids showed a significantly elevated  
478 rate of erroneous mitoses relative to controls, ranging from approximately 20% (DSS lines) to 60%  
479 (*Apc*<sup>mut</sup>) (Figure 4D-E). In addition, the mean overall time of mitosis was significantly increased in DSS  
480 control, DSS iEGFR, and *Apc*<sup>mut</sup> organoids compared to control colonoids (Figure 4H), mostly driven by  
481 increased length of nuclear envelope breakdown to chromosome alignment (Figure 4F-G).

482 Interestingly, altered mitotic timing was observed in DSS and *Apc*<sup>mut</sup> lines but not in controls (Figure 4F-  
483 H), suggesting defects in the spindle assembly checkpoint in these colonoids.

484 Finally, live imaging revealed a normal pattern of INM in most control colonoids undergoing mitosis  
485 (Figure 5A), as previously described<sup>14</sup>. In contrast, this process was conspicuously absent in many  
486 iEGFR, DSS control, DSS iEGFR, and *Apc*<sup>mut</sup> mitoses (Figure 5A). Further, INM loss was significantly  
487 associated with mitotic errors in our colonoid lines (Figure 5B-C).

488 Taken together, these data demonstrate that adaptation to long-term EGF withdrawal is associated with  
489 mitotic defects that result in chromosomal instability and aneuploidy. In addition, we associate loss of  
490 interkinetic nuclear migration with mitotic errors in colonic epithelium. Our data also show that prior  
491 chronic mucosal injury predisposes to epithelial chromosomal instability that persists *ex vivo*.

492

493

494

495

496

497

498

499

500

501

502

503

504

505

506



## 507 DISCUSSION

508 Here, using long-term selective culture, we demonstrate that normal colonoids can adapt to withdrawal  
509 of the critical niche factor EGF, a process associated with cytomorphologic features of dysplasia, loss  
510 of INM, aneuploidy, CIN, somatic deleterious mutations, and transcriptional reprogramming. These data  
511 support a scenario in which epithelial-autonomous molecular changes known to be associated with  
512 neoplasia can arise during adaptation, the acquisition of which are accelerated by prior mucosal injury.

513

514 We discovered that iEGFR colonoids show aneuploidy and CIN (Figure 4) and are primed to adapt to  
515 other niche-relevant selective pressures (Figure 1B). Genomic copy number changes were recently  
516 shown to precede chronic inflammation-associated esophageal adenocarcinoma up to a decade prior  
517 to histologic evidence of transformation<sup>45</sup>, supporting an early initiating role for genomic instability.  
518 Recent work has demonstrated low levels of spontaneous cell fusions (as we observed in iEGFR lines)  
519 in cancer cell lines that led to increased phenotypic plasticity and accelerating adaptive potential<sup>46</sup>.  
520 Future work will determine whether CIN has a causal role in mediating iEGFR tolerance.

521

522 Carroll et al. demonstrated that INM is an important homeostatic mechanism involved in directing long-  
523 term cell positioning in the intestinal crypt<sup>14</sup>. While approximately one third of normal mitoses with intact  
524 INM led to separation of mitotic sisters, mitotic sisters always remained direct neighbors in the setting of  
525 *Apc* mutation, potentially contributing to clonal expansion of early adenomas. Our data validate their  
526 finding of INM loss with *Apc* mutation, which we further extend by associating INM loss with mitotic  
527 errors in colonoid lines (Figure 5). While our live imaging data precluded definitive evaluation of post-  
528 mitotic sister cell placement, it is possible that INM loss renders cells with mitotic errors more likely to  
529 undergo clonal expansion.

530

531 Inflammation and mucosal injury reprograms colonic epithelium to a regenerative/progenitor-like  
532 status<sup>47-49</sup>, and in other organ systems, stem cell lineage infidelity drives both wound repair  
533 (homeostatic) and cancer (pathogenic)<sup>50,51</sup>. Consistent with this literature, chronic DSS colonoids  
534 showed enhanced adaptive potential to iEGFR selective culture (Figure 1A). In addition, we found  
535 polyploidy in DSS colonoids, which has also been previously reported in the setting of wound repair  
536 (Figure 4A-B)<sup>52,53</sup>. Our RNA-sequencing analysis revealed that genes related to pyroptosis were  
537 significantly upregulated in iEGFR lines (Figure 2C-D). Pyroptosis, a caspase-dependent form of  
538 proinflammatory programmed cell death, has emerging roles in the tumor microenvironment and has  
539 been recently implicated in promoting colitis-associated cancer<sup>54,55</sup>. Recent investigation of somatic

540 evolution in IBD colonic epithelium revealed clonal expansions of mutations in the IL-17 pathway which  
541 render epithelium resistant to the IL-17A-induced pro-apoptotic response<sup>56,57</sup>. Whether aneuploidy  
542 similarly confers resistance to pyroptosis-associated cell death is a future avenue of exploration.

543

544 Prior studies indicate that human adenoma-derived colonoids are uniformly dependent on EGF in  
545 culture, similar to normal colonoids<sup>3</sup>. We were surprised to find that, in contrast to wild-type control  
546 colonoids, *Apc*<sup>mut</sup> colonoids were not able to overcome withdrawal of EGF (Figure 1A). While it is well  
547 known that *KRAS/PIK3CA* wild-type CRC is susceptible to EGFR inhibition<sup>58</sup>, our data suggest that this  
548 response may also be *APC* mutation-dependent.

549

550 Recent literature has demonstrated the presence of age-associated somatic mutations in normal non-  
551 dysplastic colonic epithelium across the lifespan with uncertain consequences<sup>59-61</sup>. Although rare  
552 patients with CRC harbor alterations in the somatically mutated genes we observed in iEGFR  
553 colonoids, whether these mutations act as drivers versus passengers in the adaptive iEGFR phenotype  
554 remains to be determined. We also acknowledge that bulk exome DNA sequencing may not detect rare  
555 mutations or mutations in regulatory elements that may contribute to the phenotype of our  
556 heterogeneous iEGFR colonoid lines.

557

558 Although further work is required to elucidate a potential role for perturbed niche homeostasis in human  
559 CRC initiation, our data support a potential role for microenvironmental selective pressures in  
560 promoting neoplastic transformation. Thus, increasing the granularity of our understanding of colon  
561 anatomic segment-specific mucosal microenvironments may reveal insights into the origins of distinct  
562 pathways of tumorigenesis (for example, the serrated versus adenomatous pathways of carcinogenesis  
563 in the proximal vs. distal colon, respectively).

564

565 In summary, we leveraged murine colonoids to demonstrate that sustained deprivation of niche-  
566 relevant growth factors alone can molecularly reprogram colonic epithelium. We anticipate that there  
567 are a spectrum of mechanisms epithelia can draw upon to adapt to such selective conditions. Tracking  
568 individual clones over time and extending our approaches to human and IBD-derived colonoid lines  
569 may determine whether adaptation mechanisms such as CIN are observed more broadly. Further,  
570 elucidating the mechanisms by which neoplasia-promoting epithelial phenotypes arise may reveal  
571 general vulnerabilities attractive for cancer prevention.

572

573

## REFERENCES

574

575

576

577

578

579

580

581

582

583

584

585

586

587

588

589

590

591

592

593

594

595

596

597

598

599

600

601

602

603

604

605

606

607

608

609

610

611

612

613

614

615

616

617

618

619

620

621

622

623

624

1. Basak, O. *et al.* Induced Quiescence of Lgr5+ Stem Cells in Intestinal Organoids Enables Differentiation of Hormone-Producing Enteroendocrine Cells. *Cell Stem Cell* **20**, 177-190.e4 (2017).
2. Muzny, D. M. *et al.* Comprehensive molecular characterization of human colon and rectal cancer. *Nature* **487**, 330–337 (2012).
3. Fujii, M. *et al.* A Colorectal Tumor Organoid Library Demonstrates Progressive Loss of Niche Factor Requirements during Tumorigenesis. *Cell Stem Cell* **18**, 827–838 (2016).
4. Clevers, H. The intestinal crypt, a prototype stem cell compartment. *Cell* **154**, 274–84 (2013).
5. Powell, D. W., Pinchuk, I. V., Saada, J. I., Chen, X. & Mifflin, R. C. Mesenchymal Cells of the Intestinal Lamina Propria. *Annu. Rev. Physiol.* (2011) doi:10.1146/annurev.physiol.70.113006.100646.
6. Valenta, T. *et al.* Wnt Ligands Secreted by Subepithelial Mesenchymal Cells Are Essential for the Survival of Intestinal Stem Cells and Gut Homeostasis. *Cell Rep.* **15**, 911–918 (2016).
7. Sato, T. *et al.* Long-term Expansion of Epithelial Organoids From Human Colon, Adenoma, Adenocarcinoma, and Barrett's Epithelium. *Gastroenterology* **141**, 1762–1772 (2011).
8. van de Wetering, M. *et al.* Prospective Derivation of a Living Organoid Biobank of Colorectal Cancer Patients. *Cell* **161**, 933–945 (2015).
9. Kobayashi, H. *et al.* The balance of stromal BMP signaling mediated by GREM1 and ISLR drives colorectal carcinogenesis. *Gastroenterology* (2020) doi:10.1053/j.gastro.2020.11.011.
10. Drost, J. *et al.* Sequential cancer mutations in cultured human intestinal stem cells. *Nature* **521**, 43–47 (2015).
11. Matano, M. *et al.* Modeling colorectal cancer using CRISPR-Cas9-mediated engineering of human intestinal organoids. *Nat. Med.* **21**, 256–262 (2015).
12. Li, X. *et al.* Oncogenic transformation of diverse gastrointestinal tissues in primary organoid culture. *Nat. Med.* **20**, 769–777 (2014).
13. Ritsma, L. *et al.* Intestinal crypt homeostasis revealed at single-stem-cell level by in vivo live imaging. *Nature* **507**, 362–365 (2014).
14. Carroll, T. D. *et al.* Interkinetic nuclear migration and basal tethering facilitates post-mitotic daughter separation in intestinal organoids. *J. Cell Sci.* **130**, 3862–3877 (2017).
15. Kinchen, J. *et al.* Structural Remodeling of the Human Colonic Mesenchyme in Inflammatory Bowel Disease. *Cell* **175**, 372-386.e17 (2018).
16. Colotta, F., Allavena, P., Sica, A., Garlanda, C. & Mantovani, A. Cancer-related inflammation, the seventh hallmark of cancer: links to genetic instability. *Carcinogenesis* **30**, 1073–1081 (2009).
17. Coussens, L. M. & Werb, Z. Inflammation and cancer. *Nature* **420**, 860–867 (2002).
18. Holloway, E. M. *et al.* Mapping Development of the Human Intestinal Niche at Single-Cell Resolution. *Cell Stem Cell* (2020) doi:10.1016/j.stem.2020.11.008.
19. Fawkner-Corbett, D. *et al.* Spatiotemporal analysis of human intestinal development at single-cell resolution. *Cell* S009286742031686X (2021) doi:10.1016/j.cell.2020.12.016.
20. Ovid: Peptide growth factors in the intestine. <http://ovidsp.dc2.ovid.com/ovid-b/ovidweb.cgi?T=JS&PAGE=fulltext&D=ovft&AN=00042737-200107000-00002&CHANNEL=CrossRef>.
21. Eichele, D. D. & Kharbanda, K. K. Dextran sodium sulfate colitis murine model: An indispensable tool for advancing our understanding of inflammatory bowel diseases pathogenesis. *World J. Gastroenterol.* **23**, 6016–6029 (2017).
22. Chassaing, B., Aitken, J. D., Malleshappa, M. & Vijay-Kumar, M. Dextran sulfate sodium (DSS)-induced colitis in mice. *Curr. Protoc. Immunol.* **104**, 15.25.1-15.25.14 (2014).
23. Wirtz, S. *et al.* Chemically induced mouse models of acute and chronic intestinal inflammation. *Nat. Protoc.* **12**, 1295–1309 (2017).
24. Sato, T. *et al.* Paneth cells constitute the niche for Lgr5 stem cells in intestinal crypts. *Nature* **469**, 415–8 (2011).

- 625 25. Drost, J. *et al.* Sequential cancer mutations in cultured human intestinal stem cells. *Nature* **521**, 43–  
626 47 (2015).
- 627 26. Schwank, G. & Clevers, H. CRISPR/Cas9-Mediated Genome Editing of Mouse Small Intestinal  
628 Organoids. in *Gastrointestinal Physiology and Diseases: Methods and Protocols* (ed. Ivanov, A. I.)  
629 3–11 (Springer, 2016). doi:10.1007/978-1-4939-3603-8\_1.
- 630 27. Dekkers, J. F. *et al.* High-resolution 3D imaging of fixed and cleared organoids. *Nat. Protoc.* **14**,  
631 1756–1771 (2019).
- 632 28. Bolhaqueiro, A. C. F. *et al.* Live imaging of cell division in 3D stem-cell organoid cultures. in (2018).  
633 doi:10.1016/bs.mcb.2018.03.016.
- 634 29. Miura, K. *Temporal-Color Code (Version 101123)*  
635 [https://github.com/fiji/fiji/blob/master/plugins/Scripts/Image/Hyperstacks/Temporal-Color\\_Code.ijm](https://github.com/fiji/fiji/blob/master/plugins/Scripts/Image/Hyperstacks/Temporal-Color_Code.ijm)  
636 (2010).
- 637 30. Pavelka, N. *et al.* Aneuploidy confers quantitative proteome changes and phenotypic variation in  
638 budding yeast. *Nature* **468**, 321–325 (2010).
- 639 31. Dobin, A. *et al.* STAR: ultrafast universal RNA-seq aligner. *Bioinforma. Oxf. Engl.* **29**, 15–21 (2013).
- 640 32. Liao, Y., Smyth, G. K. & Shi, W. The Subread aligner: fast, accurate and scalable read mapping by  
641 seed-and-vote. *Nucleic Acids Res.* **41**, e108 (2013).
- 642 33. Love, M. I., Huber, W. & Anders, S. Moderated estimation of fold change and dispersion for RNA-  
643 seq data with DESeq2. *Genome Biol.* **15**, 550 (2014).
- 644 34. Raudvere, U. *et al.* g:Profiler: a web server for functional enrichment analysis and conversions of  
645 gene lists (2019 update). *Nucleic Acids Res.* **47**, W191–W198 (2019).
- 646 35. Kim, J. J., Shajib, M. S., Manocha, M. M. & Khan, W. I. Investigating intestinal inflammation in DSS-  
647 induced model of IBD. *J. Vis. Exp. JoVE* (2012) doi:10.3791/3678.
- 648 36. Nowak, M. A. *et al.* The role of chromosomal instability in tumor initiation. *Proc. Natl. Acad. Sci. U.*  
649 *S. A.* **99**, 16226–16231 (2002).
- 650 37. Moniz, S. *et al.* Protein kinase WNK2 inhibits cell proliferation by negatively modulating the  
651 activation of MEK1/ERK1/2. *Oncogene* **26**, 6071–6081 (2007).
- 652 38. James, R. G. *et al.* Bruton's tyrosine kinase revealed as a negative regulator of Wnt-beta-catenin  
653 signaling. *Sci. Signal.* **2**, ra25 (2009).
- 654 39. Yasuda, Y. *et al.* Human NINEIN polymorphism at codon 1111 is associated with the risk of  
655 colorectal cancer. *Biomed. Rep.* **13**, 1–1 (2020).
- 656 40. Fischer, A. H. *et al.* The cytologic criteria of malignancy. *J. Cell. Biochem.* **110**, 795–811 (2010).
- 657 41. Hanahan, D. & Weinberg, R. A. *Hallmarks of cancer: The next generation.* *Cell* vol. 144 (2011).
- 658 42. Rancati, G. *et al.* Aneuploidy Underlies Rapid Adaptive Evolution of Yeast Cells Deprived of a  
659 Conserved Cytokinesis Motor. *Cell* **135**, 879–893 (2008).
- 660 43. Huch, M. & Koo, B.-K. Modeling mouse and human development using organoid cultures.  
661 *Development* **142**, 3113–3125 (2015).
- 662 44. Rusan, N. M. & Peifer, M. Original CIN: reviewing roles for APC in chromosome instability. *J. Cell*  
663 *Biol.* **181**, 719–726 (2008).
- 664 45. Killcoyne, S. *et al.* Genomic copy number predicts esophageal cancer years before transformation.  
665 *Nat. Med.* **26**, 1726–1732 (2020).
- 666 46. Miroshnychenko, D. *et al.* Spontaneous cell fusions as a mechanism of parasexual recombination  
667 in tumour cell populations. *Nat. Ecol. Evol.* 1–13 (2021) doi:10.1038/s41559-020-01367-y.
- 668 47. Schwitalla, S. *et al.* Intestinal Tumorigenesis Initiated by Dedifferentiation and Acquisition of Stem-  
669 Cell-like Properties. *Cell* **152**, 25–38 (2013).
- 670 48. Miyoshi, H. *et al.* Prostaglandin E2 promotes intestinal repair through an adaptive cellular response  
671 of the epithelium. *EMBO J.* **36**, 5–24 (2017).
- 672 49. Yui, S. *et al.* YAP/TAZ-Dependent Reprogramming of Colonic Epithelium Links ECM Remodeling to  
673 Tissue Regeneration. *Cell Stem Cell* **22**, 35-49.e7 (2018).
- 674 50. Dvorak, H. F. Tumors: Wounds That Do Not Heal—Redux. *Cancer Immunol. Res.* **3**, 1–11 (2015).

- 675 51. Ge, Y. *et al.* Stem Cell Lineage Infidelity Drives Wound Repair and Cancer. *Cell* **169**, 636-650.e14  
676 (2017).
- 677 52. Losick, V. P. Wound-Induced Polyploidy Is Required for Tissue Repair. *Adv. Wound Care* **5**, 271–  
678 278 (2016).
- 679 53. Lucchetta, E. M. & Ohlstein, B. Amitosis of Polyploid Cells Regenerates Functional Stem Cells in  
680 the *Drosophila* Intestine. *Cell Stem Cell* **20**, 609-620.e6 (2017).
- 681 54. Tan, G., Huang, C., Chen, J. & Zhi, F. HMGB1 released from GSDME-mediated pyroptotic  
682 epithelial cells participates in the tumorigenesis of colitis-associated colorectal cancer through the  
683 ERK1/2 pathway. *J. Hematol. Oncol.* *J Hematol Oncol* **13**, 149 (2020).
- 684 55. Xia, X. *et al.* The role of pyroptosis in cancer: pro-cancer or pro-“host”? *Cell Death Dis.* **10**, 650  
685 (2019).
- 686 56. Olafsson, S. *et al.* Somatic Evolution in Non-neoplastic IBD-Affected Colon. *Cell*  
687 S0092867420308138 (2020) doi:10.1016/j.cell.2020.06.036.
- 688 57. Nanki, K. *et al.* Somatic inflammatory gene mutations in human ulcerative colitis epithelium. *Nature*  
689 **577**, 254–259 (2020).
- 690 58. Khan, K. *et al.* Targeting EGFR pathway in metastatic colorectal cancer- tumour heterogeneity and  
691 convergent evolution. *Crit. Rev. Oncol. Hematol.* **143**, 153–163 (2019).
- 692 59. Lee-Six, H. *et al.* The landscape of somatic mutation in normal colorectal epithelial cells. *Nature*  
693 **574**, 532–537 (2019).
- 694 60. Nicholson, A. M. *et al.* Fixation and Spread of Somatic Mutations in Adult Human Colonic  
695 Epithelium. *Cell Stem Cell* **22**, 909-918.e8 (2018).
- 696 61. Smith, A. L. M. *et al.* Age-associated mitochondrial DNA mutations cause metabolic remodeling that  
697 contributes to accelerated intestinal tumorigenesis. *Nat. Cancer* **1**, 976–989 (2020).
- 698
- 699
- 700
- 701
- 702
- 703
- 704
- 705
- 706
- 707
- 708
- 709
- 710
- 711
- 712
- 713

714 **FIGURE LEGENDS**

715 **Figure 1. Colonoids adapt to culture conditions devoid of critical niche factors.**

716 **A)** Survival rate depicting viability of colonoids at the end of each selection cycle (7 days) as a  
717 percentage of colonoid growth in control media (n= 6 biological replicates). **B)** Survival rate of colonoid  
718 lines in other selective media after 7 days (n=3 biological replicates), \*\*\*\* $p < 0.0001$ , 2-tailed non-  
719 paired student t-test.

720

721 **Figure 2. Long-term adaptation of colonoids to EGF-deficient conditions results in**  
722 **transcriptional changes.**

723 **A)** Samples analyzed by RNA-seq were plotted by principal component 1 (PC1) and principal  
724 component 2 (PC2) using raw count data following regularized logarithm transformation. Samples from  
725 the same experimental condition were grouped with the same colors. **B)** Volcano plots displaying  $\log_2$ -  
726 transformed fold change and  $-\log_{10}$ -transformed  $p$  value of genes assessed by RNA-seq in iEGFR vs.  
727 control colonoids and DSS iEGFR vs. DSS control colonoids. Selected differentially expressed genes  
728 are highlighted. Genes highlighted in green are differentially expressed in both iEGFR and DSS iEGFR  
729 compared to the respective control. Genes highlighted in red and blue are differentially expressed only  
730 in iEGFR or DSS iEGFR, respectively. **C)** Gene set enrichment analysis of overlapping upregulated and  
731 downregulated genes in both iEGFR and DSS iEGFR compared to the respective control. All enriched  
732 gene sets ( $p$  value  $< 0.05$ ) are shown. **D)** Quantitative RT-PCR validation of select upregulated (left)  
733 and downregulated (right) genes detected by RNA-seq. Results are expressed as  $\log_2$  fold change to  
734 control and DSS control (n=3).

735

736 **Figure 3. iEGFR colonoids show morphologic features of dysplasia and increased proliferation.**

737 **A)** Representative H&E stained human tissues (upper panels, 20X) and cultured colonoids (lower  
738 panels, 40X). Squares denote nuclear hyperchromasia and loss of nuclear polarity, arrowheads denote  
739 architectural complexity, asterisks denote squamous features, and the triangle denotes overall normal  
740 epithelial morphology. **B)** Representative confocal maximal Z-stacks images for colonoids stained with  
741 the thymidine analogue EdU (green) and the counterstain DAPI (blue). No-EdU and Nutlin served as  
742 negative and positive controls, respectively. Scale bars = 50  $\mu\text{m}$ . n = 3 independent experiments. **C)**  
743 Box and whiskers plot for the percentage of EdU positive nuclei per EdU-positive colonoid. Transverse  
744 lines represent the median, boxes show 25<sup>th</sup>-75<sup>th</sup> percentile and the whiskers represent the lowest and  
745 highest values within 1.5 times the interquartile range. \*\*\*\* $p < 0.0001$ , \* $p \leq 0.05$ ; 2-tailed, non-paired  
746 student t-test. **D)** Bar plot for the percentage of colonoids with at least one EdU positive cell (n= 3

747 biological replicates). Error bars represent standard deviation. \*\*\*\* $p < 0.0001$ , \* $p \leq 0.05$ ; 2-tailed, non-  
748 paired student t-test.

749

750 **Figure 4. iEGFR colonoids are aneuploid and demonstrate chromosomal instability.**

751 **A)** Dot plot of the number of chromosomes in metaphase spreads. The number of counted spreads and  
752 the percentage of metaphase spreads with euploid chromosomes are shown at the top. The red line  
753 represents tetraploidy. iEGFR(H) and iEGFR(L) correspond to high passage number ('H' high, passage  
754 66) and lower passage number ('L' low, passage 40), respectively. **B)** Representative images of  
755 metaphase spreads from control (euploid) and DSS control (tetraploid) colonoids. 60x. **C)**  
756 Representative color depth coded images of chromosome segregation errors as revealed by H2B-  
757 mNeon labeling of colonoids. Insets highlight mitoses in white boxes. White arrows indicate mitotic  
758 errors, corresponding to Supplementary Videos 1-6.  $n = 4$  or  $5$  independent experiments. **D)** Box and  
759 whiskers plot of the percentage of segregation errors. Transverse lines represent the median, boxes  
760 show 25<sup>th</sup>-75<sup>th</sup> percentile and the whiskers represent the lowest and highest values within 1.5 times the  
761 interquartile range. The number of divisions and colonoids analyzed are shown at the top.  
762 \*\*\*\* $p < 0.0001$ , \* $p \leq 0.05$ ; 2-tailed, non-paired student t-test. **E)** Bar plot of the percentage of different  
763 segregation errors in analyzed mitotic figures. Other types of errors include multipolar mitoses, mitotic  
764 failure, and fusion of nuclei. **F-H)** Illustrative cartoons and violin plots for time distribution of duration  
765 from nuclear envelope breakdown (NEB) to chromosome alignment (F), chromosome alignment to  
766 completion of mitosis (G), and total mitotic time (H). Transverse solid lines represent the median and  
767 the dotted lines border 25<sup>th</sup> -75<sup>th</sup> percentiles. \*\*\*\* $p < 0.0001$ , \* $p \leq 0.05$ ; 2-tailed, non-paired student t-  
768 test.

769

770 **Figure 5. INM loss is frequent in iEGFR colonoids and significantly associated with mitotic**  
771 **errors.**

772 **A)** Sequential still images captured from representative individual mitoses (highlighted by white  
773 arrowheads) as revealed by H2B-mNeon labeling of control, iEGFR, and *Apc*<sup>mut</sup> colonoids. **B)** Bar  
774 graph stratifying the presence of mitotic errors with the presence ( $n=79$ ) or loss ( $n=98$ ) of INM in all  
775 analyzed mitoses across colonoid lines. \*\*\*\* $p < 0.0001$ ; 2-tailed Fisher's exact test. **C)** Bar graph  
776 detailing the percentage of mitoses with INM loss in each colonoid line. The number of mitoses and  
777 colonoids evaluated per group are shown at top. \*\*\* $p < 0.001$ , \* $p \leq 0.05$ ; 2-tailed Fisher's exact test.

778

779 **Table 1. iEGFR colonoids acquire rare high-impact protein-coding mutations.**

780 **SUPPLEMENTARY FIGURES, TABLES, AND VIDEOS**

781

782 **Supplementary Figure 1. A)** Representative confocal fluorescence images (Z sections with maximum  
783 projection) of cleared colonoids labeled with chromogranin A (CHGA, green) and the counter stain  
784 DAPI (blue). **B)** Bar plot illustrating the number of chromogranin A positive cells per colonoid, evidence  
785 of enteroendocrine differentiation. Error bars represent standard deviation. \*\*\*  $p < 0.001$ . **C)** Bar plot  
786 demonstrating the survival rate of iEGFR colonoids after re-challenging with iEGFR and other selective  
787 media after 3 weeks in EGF-replete media, relative to control.

788

789 **Supplementary Figure 2. A)** Bar plot for the ratio of body weight to colon length in mice treated with  
790 DSS in water vs. water only control. Error bars represents standard deviation.  $n=3$ . **B)** Representative  
791 H&E sections of colons from a DSS-treated (right) and a control mouse (left).

792

793 **Supplementary Figure 3. A)** Targeting sites and sgRNA that were used to target *Apc* in normal mouse  
794 colonoids. **B)** Whole exome sequencing of *Apc*<sup>mut</sup> colonoids confirms the presence of biallelic truncating  
795 mutations at the expected site of targeted CRISPR/Cas9 genome editing. **C)** Representative brightfield  
796 images of *Apc*<sup>mut</sup> colonoids with characteristic spheroid morphology, as well as representative image  
797 from other colonoid lines. **D)** Representative brightfield images of colonoid lines corresponding to Day 0  
798 and Day 7 of the selective challenges detailed in Figure 1B.

799

800 **Supplementary Figure 4.** The number of differentially expressed genes in iEGFR colonoids relative to  
801 control organoids,  $\log_2$  fold changes  $\geq 2$  and Bonferroni  $p$ -value  $< 0.05$ . **A)** upregulated genes, **B)**  
802 downregulated genes.

803

804 **Supplementary Figure 5.** Chromosome copy number in control (euploid) and higher-passage iEGFR  
805 colonoids (~passage 54, aneuploid) quantified by qPCR, indicating loss of one copy of chromosome  
806 13.  $n = 3$  technical replicates.

807

808 **Supplementary Figure 6. A)** Representative confocal fluorescence images (Z sections with maximum  
809 projection) of colonoids stained with  $\gamma$ H2AX antibodies (red) and DAPI (blue). Doxorubicin and No Ab  
810 (no antibody) represent the positive and negative controls, respectively. Scale bars = 50 $\mu$ m. **B)** The  
811 percentage of  $\gamma$ H2AX positive cells/colonoid is represented as a box and whisker plot. Transverse lines  
812 represent the median, boxes show 25<sup>th</sup>-75<sup>th</sup> percentile and the whiskers represent the lowest and



813 highest values within 1.5 times the interquartile range. ns = not statistically significant,  $p \geq 0.05$  2-tailed,  
814 non-paired student t-test.

815

816

817 **Supplementary Table 1.** Unfiltered differentially expressed genes in iEGFR and DSS iEGFR colonoid  
818 lines vs. their respective controls.

819 **Supplementary Table 2.** Mouse primer sequences for chromosome karyotyping by qRT-PCR.

820 **Supplementary Table 3.** Mouse primer sequences for qRT-PCR validation of RNA-seq data

821

822 **Supplementary Video 1 (Control colonoids)**

823 Example of normal cell division.

824 **Supplementary Video 2 (iEGFR colonoids)**

825 Example of an erroneous division with a multipolar mitosis.

826 **Supplementary Video 3 (iEGFR colonoids)**

827 Example of an erroneous division with an anaphase bridge.

828 **Supplementary Video 4 (DSS control colonoids)**

829 Example of an erroneous division with a lagging chromosome.

830 **Supplementary Video 5 (DSS iEGFR colonoids)**

831 Example of an erroneous division with mitotic failure.

832 **Supplementary Video 6 (*Apc*<sup>mut</sup> colonoids)**

833 Example of lagging chromosomes.

834

835

836

# Figure 1

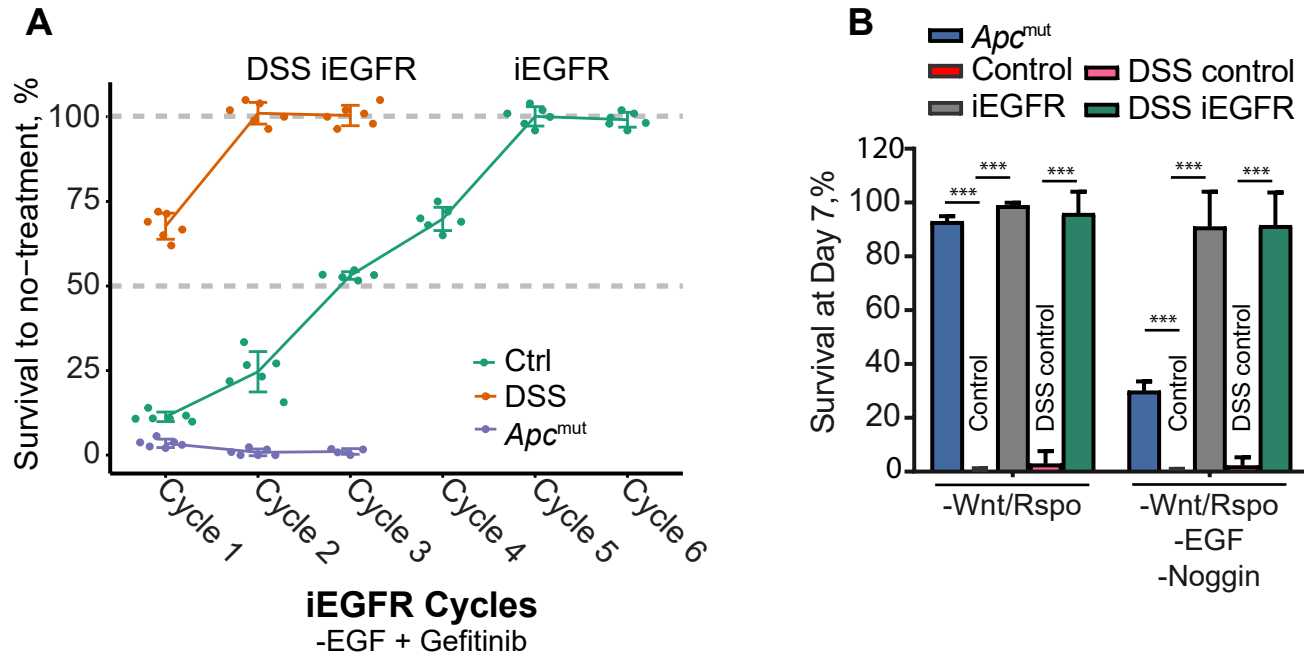


## Figure 2

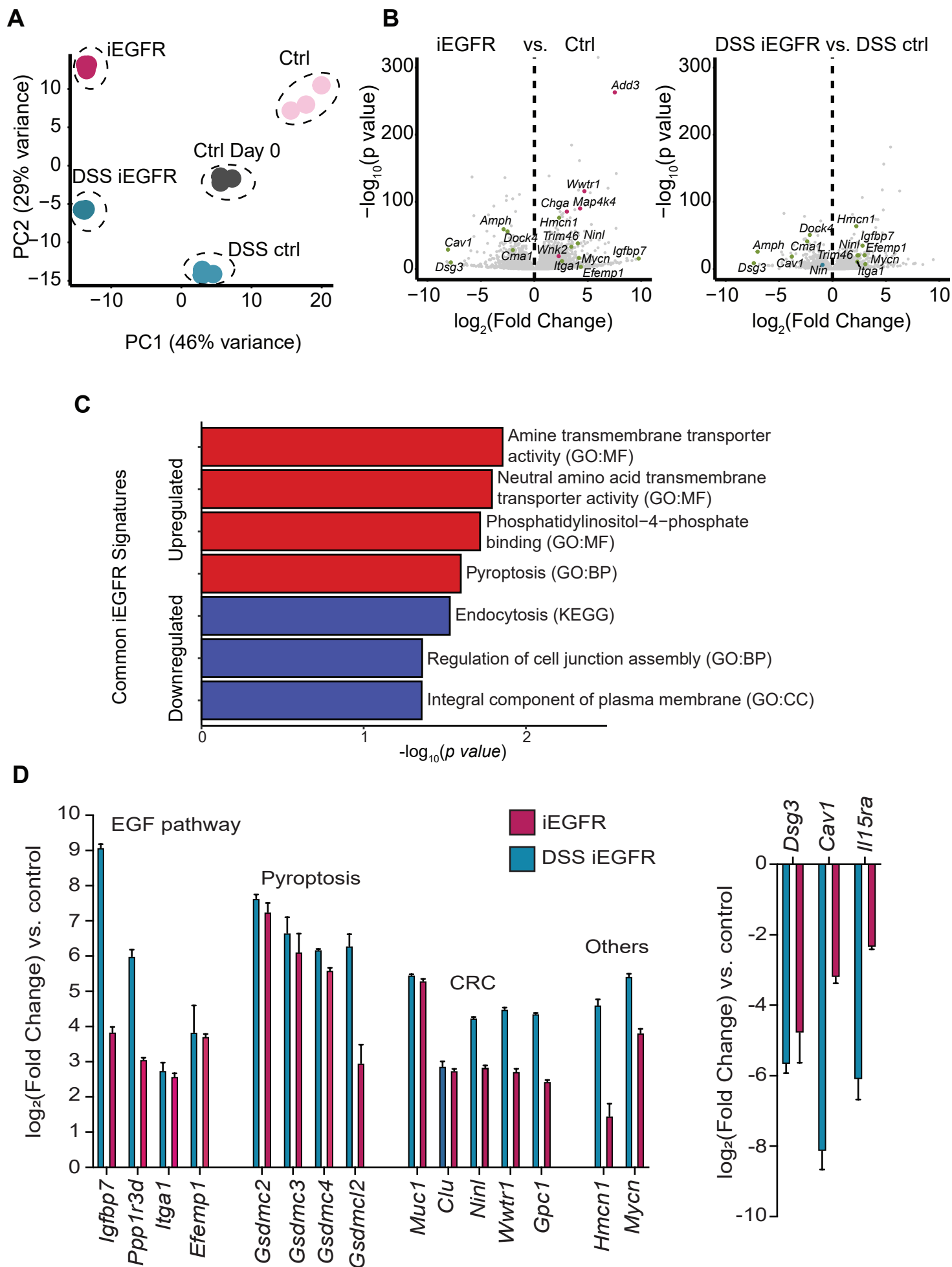
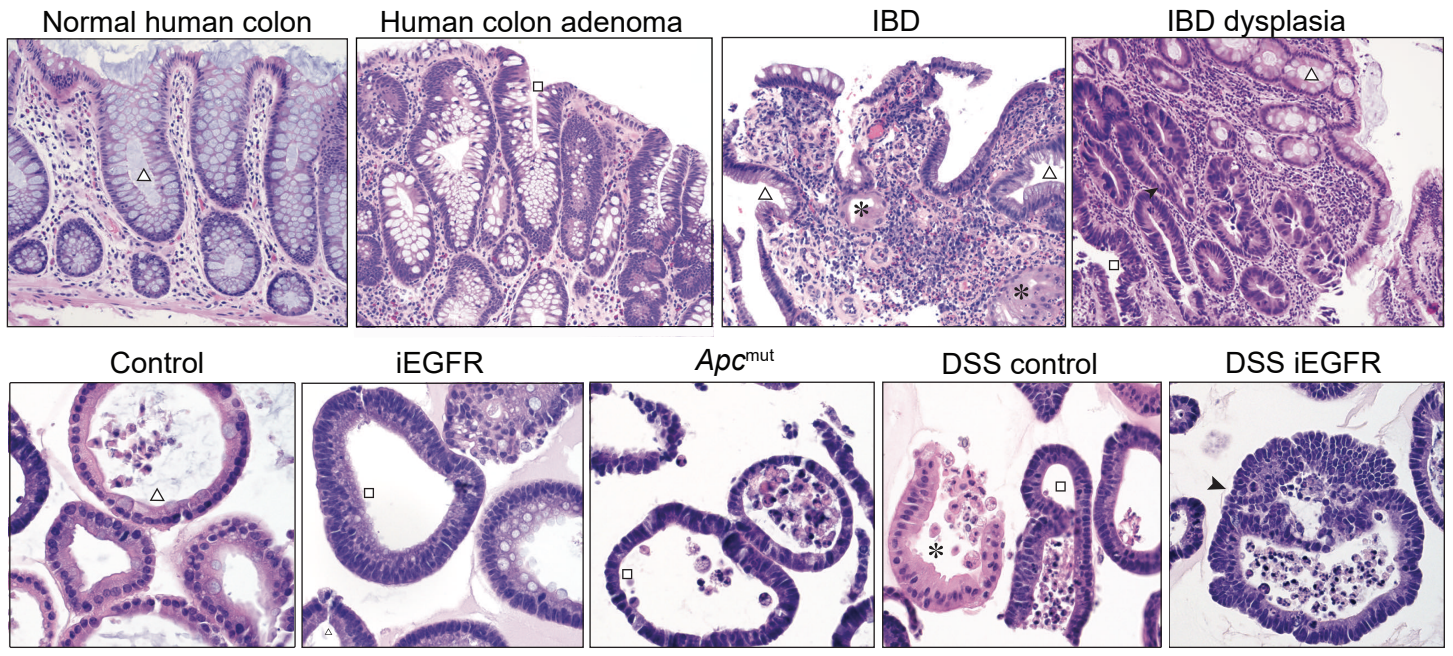
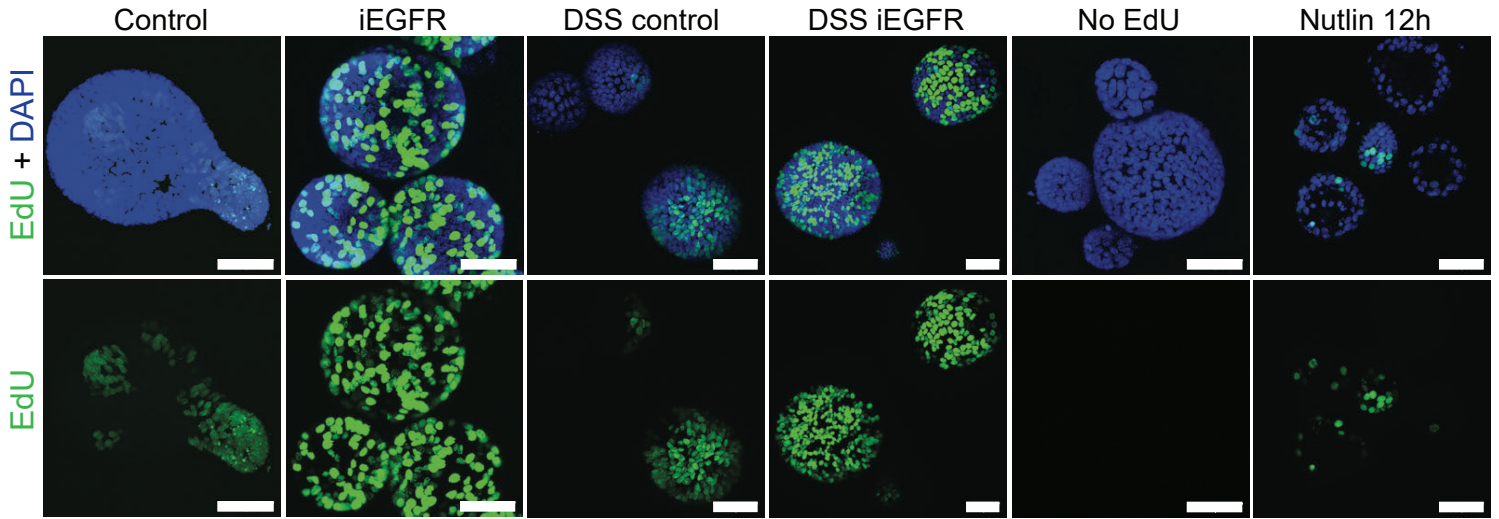


## Figure 3

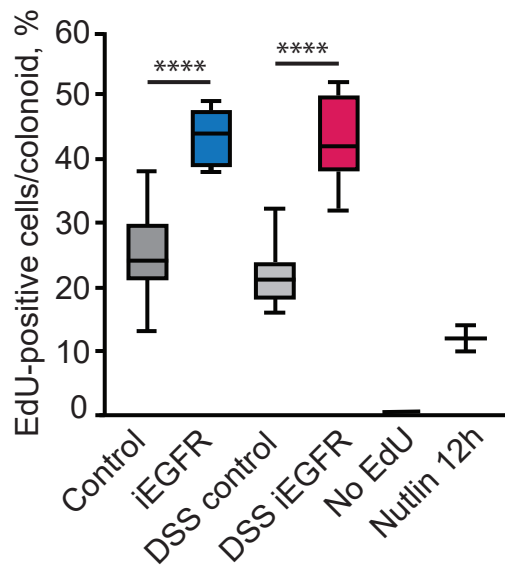
**A**



**B**



**C**



**D**

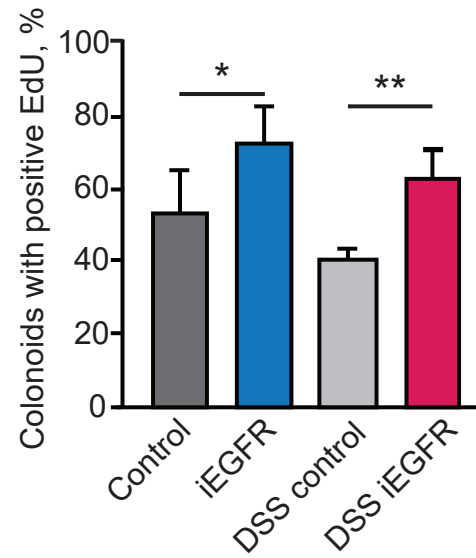


## Figure 4

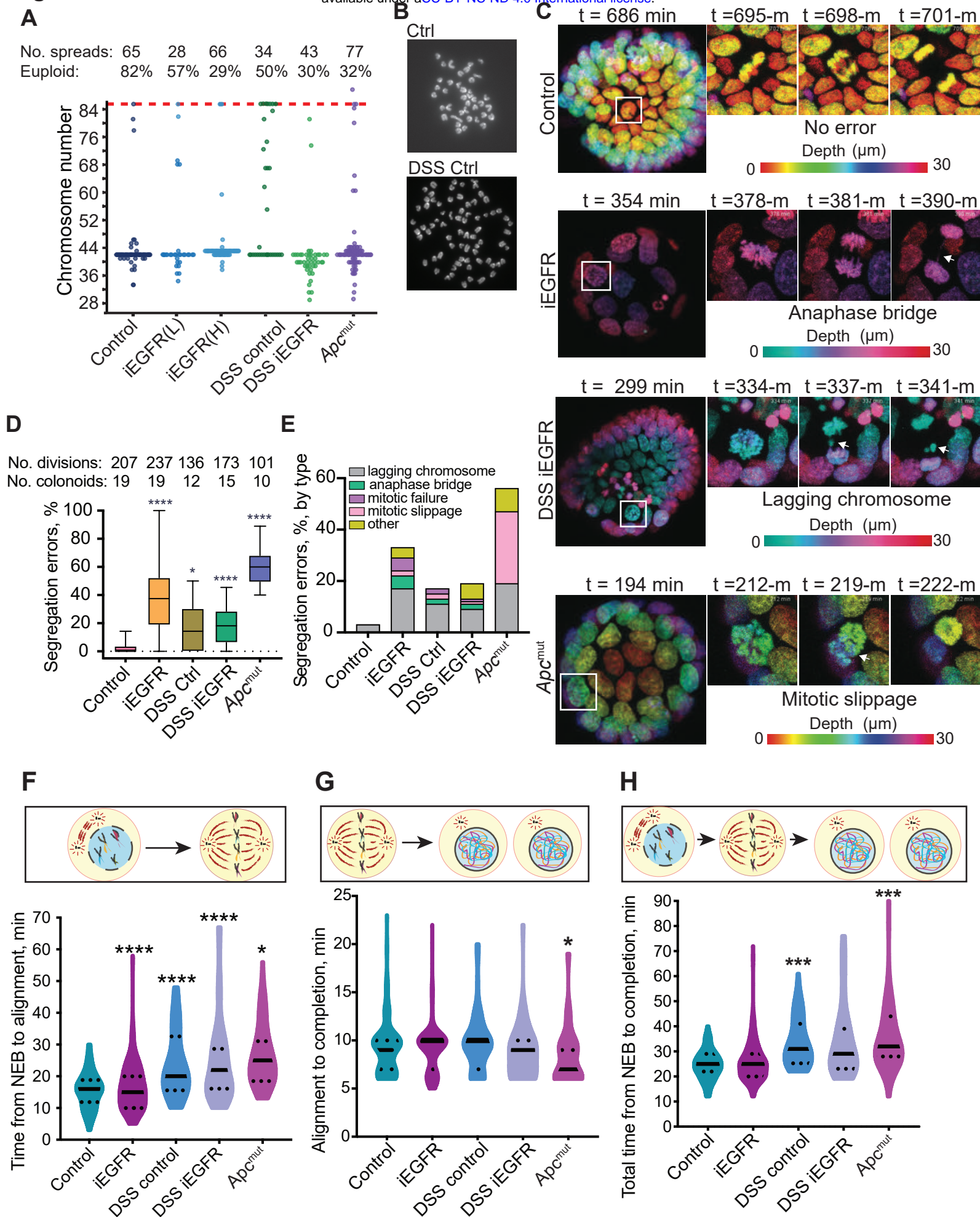


## Figure 5

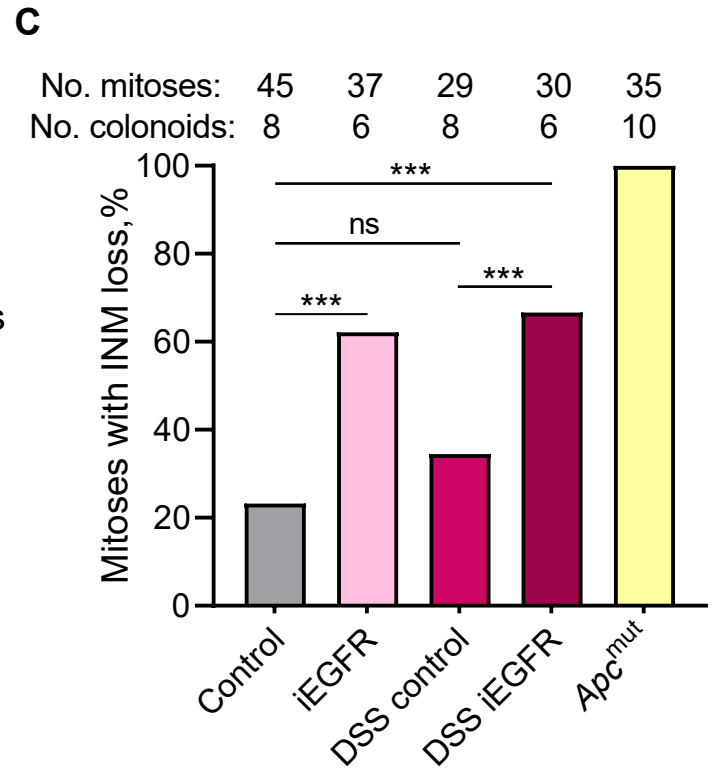
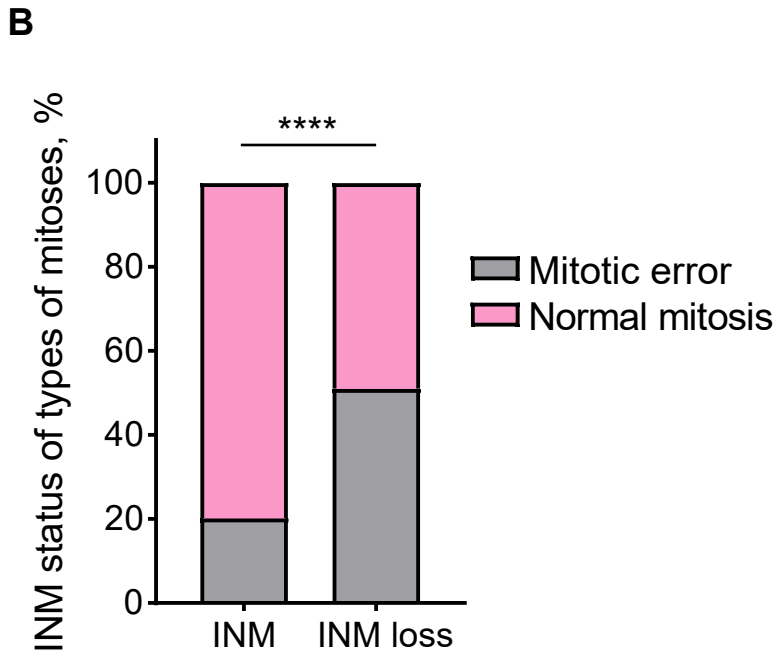
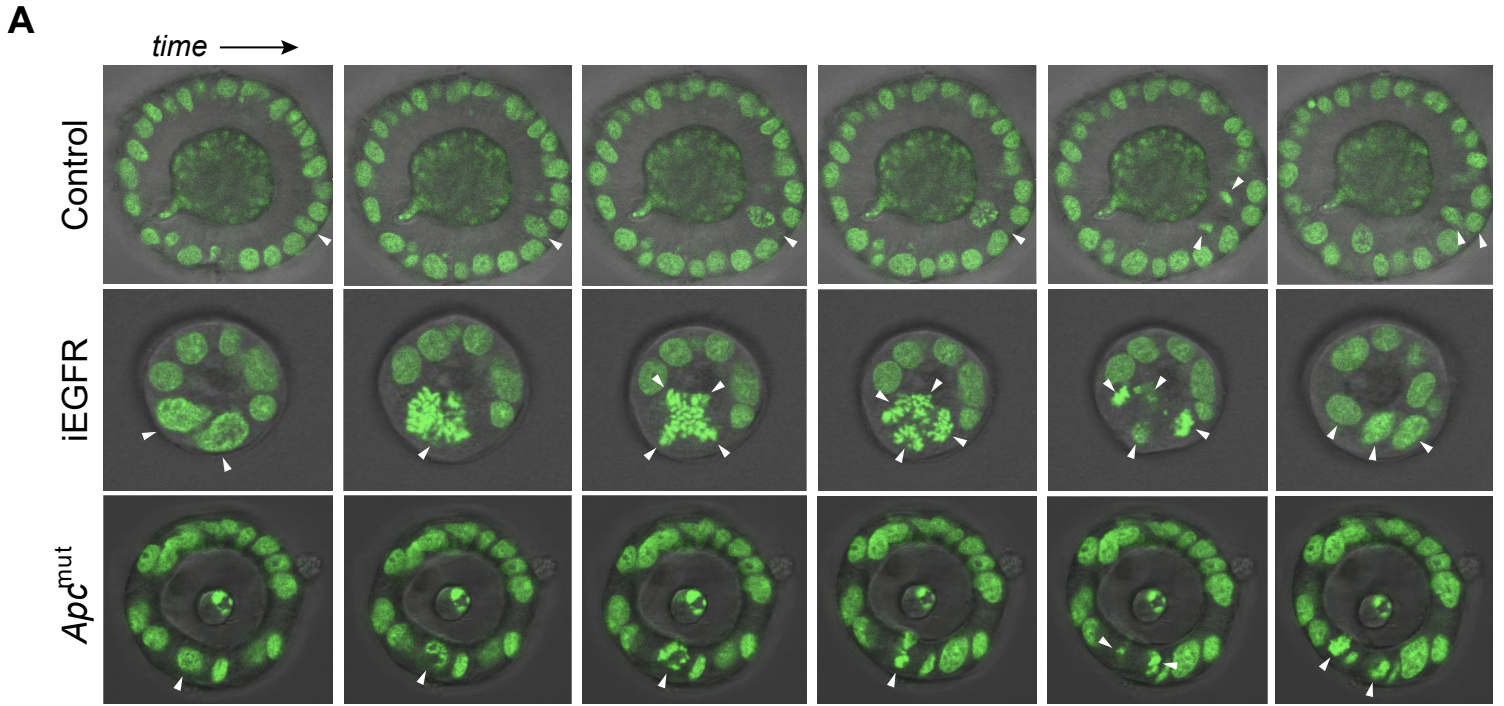


**Table 1.** Summary of mutations identified in iEGFR colonoids by WES.

Sample	Chr	Gene	Mutation	VAF (reads)	Mutation Type	Known function of gene product	Frequency of gene alteration in human CRC patients
iEGFR	X	<i>Btk</i>	p.Lys573*/c.1717A>T	48% (48/52)	Nonsense	Negative regulator of Wnt- $\beta$ -catenin signaling	26/3407 (0.8%)
iEGFR	2	<i>Olf1255</i>	p.Ile210fs/c.628_629delAT	38% (57/151)	Frameshift	Olfactory receptor	N/A
iEGFR	17	<i>Trem12</i>	p.Trp76*/c.227G>A	48% (45/93)	Nonsense	Roles in innate and adaptive immunity	1/3407 (0.03%)
iEGFR	13	<i>Wnk2</i>	p.Thr751fs/c.2249insC	60% (6/10)	Frameshift	Negative regulator of EGF-induced activation of the ERK/MAPK-pathway, cell cycle progression	5/3407 (0.1%)
DSS iEGFR	12	<i>Ninein</i>	p.Gln114*/c.340C>T	27% (31/113)	Nonsense	Centrosomal protein, microtubule anchoring	23/3407 (0.7%)

Predicted high-impact mutations detected by WES performed on iEGFR lines and respective controls. With the exception of *Ninein*, these mutations were not detected in control lines (passage matched for control). *Ninein* mutation was found at 13% VAF (12/85 reads) in the DSS control line, and at 27% VAF in DSS iEGFR (31/113 reads). Genetic alterations were queried from publicly available data in cBioPortal, and excluded germline variants and variants of unknown significance.